Neuron, Vol. 39, 27–41, July 3, 2003, Copyright ©2003 by Cell Press

All-Optical Histology Using Ultrashort Laser Pulses

Neurotechnique

Philbert S. Tsai,[1] Beth Friedman,[2] Agustin I. Ifarraguerri,[8] Beverly D. Thompson,[9] Varda Lev-Ram,[3] Chris B. Schaffer,[1] Qing Xiong,[4] Roger Y. Tsien,[3,4,5,6] Jeffrey A. Squier,[10] and David Kleinfeld[1,6,7,*]

[1]Department of Physics
[2]Department of Neurosciences
[3]Department of Pharmacology
[4]Howard Hughes Medical Institute
[5]Department of Chemistry and Biochemistry
[6]Graduate Program in Neurosciences
[7]Center for Theoretical Biological Physics
University of California, San Diego
La Jolla, California 92093
[8]Science Applications International Corporation
Arlington, Virginia 22203
[9]Science Applications International Corporation
McLean, Virginia 22102
[10]Department of Physics
Colorado School of Mines
Golden, Colorado 80401

Summary

As a means to automate the three-dimensional histological analysis of brain tissue, we demonstrate the use of femtosecond laser pulses to iteratively cut and image fixed as well as fresh tissue. Cuts are accomplished with 1 to 10 μJ pulses to ablate tissue with micron precision. We show that the permeability, immunoreactivity, and optical clarity of the tissue is retained after pulsed laser cutting. Further, samples from transgenic mice that express fluorescent proteins retained their fluorescence to within microns of the cut surface. Imaging of exogenous or endogenous fluorescent labels down to 100 μm or more below the cut surface is accomplished with 0.1 to 1 nJ pulses and conventional two-photon laser scanning microscopy. In one example, labeled projection neurons within the full extent of a neocortical column were visualized with micron resolution. In a second example, the microvasculature within a block of neocortex was measured and reconstructed with micron resolution.

Introduction

The advent of new probes for brain molecular structure has catalyzed insights into both the normal and pathological functions of the nervous system. Further advances are anticipated with the creation of transgenic mice in which the expression of individual gene products are tagged with an intrinsic optically active label. However, in contrast to the progress in methodologies that identify novel molecules, the technologies of neuroanatomy, which form the core of our ability to map cellular phenotypes, are still typically very slow. The extension of tissue histology to high throughput applications requires the type of standardization and automation that has driven similar efforts in proteomics and molecular biology. In this respect, a key limitation in the standard practice of light microscope-based histology is the need to manually obtain and transfer sections of tissue onto glass slides that are then processed in order to visualize structural and molecular components. An intriguing alternative to this section-based histology are methods where the sectioned face of the tissue block is directly imaged (Rauschning, 1986; Toga et al., 1994). Studies with this block-based histology, where the sectioning and imaging occurred iteratively, enabled the construction of atlases of the human brain (Toga et al., 1997). Furthermore, this methodology eliminates the need to register individual sections as well as correct for warpage. However, since these block-based methods require the use of frozen tissue, only a limited number of structural elements can be imaged.

Recent work in the field of ultrashort pulsed lasers supports the potential use of lasers to section or remove layers of tissue and thereby form a core method for an all-optical histology that could lend itself to automation. In particular, ultrashort laser pulses with high values of fluence, i.e., energies per unit area greater than 1 J/cm^2 as achieved by optical amplification or extremely tight focusing, have been used for the ablation of dielectics (Du et al., 1994; Lenzner et al., 1998; Stuart et al., 1995, 1996) and metals (Momma et al., 1996; Shirk and Molian, 1998) as well as biological tissues, including bone, dentine, and enamel (Neev et al., 1996); cornea (Loesel et al., 1996; Oraevsky et al., 1996; Juhasz et al., 1999; Lubatschowski et al., 2000; Maatz et al., 2000); epithelia (Frederickson et al., 1993); and brain (Loesel et al., 1998; Suhm et al., 1996; Goetz et al., 1999). The use of ultrashort laser pulses for poration at the level of single cells has recently been demonstrated (Tirlapur and Konig, 2002). This and other considerations suggest the use of ultrashort laser pulses as a tool for the precise removal of brain tissue.

The potential to use ultrashort amplified laser pulses as a histological tool is buttressed by the use of similar but nonamplified pulses of laser light in the maturing imaging technology of two-photon laser scanning microscopy (TPLSM) (Denk et al., 1990; Denk and Svoboda, 1997). TPLSM offers a powerful tool to accelerate the acquisition of histological data because it provides the capacity to image fluorescent molecules to depths of hundreds of microns from the surface of the brain (Kleinfeld et al., 1998; Oheim et al., 2001), which reduces the number of samples that must be prepared for imaging. The photo-dynamic damage from imaging with TPLSM is sufficiently low that it has been possible to use this modality for in vivo functional imaging of dendritic spines that are tagged with fluorescent probes (Grutzendler et al., 2002; Lendvai et al., 2000; Svoboda et al., 1997; Yuste and Denk, 1995). Thus, the combined use of amplified ultrashort laser pulses to ablate tissue and

*Correspondence: dk@physics.ucsd.edu

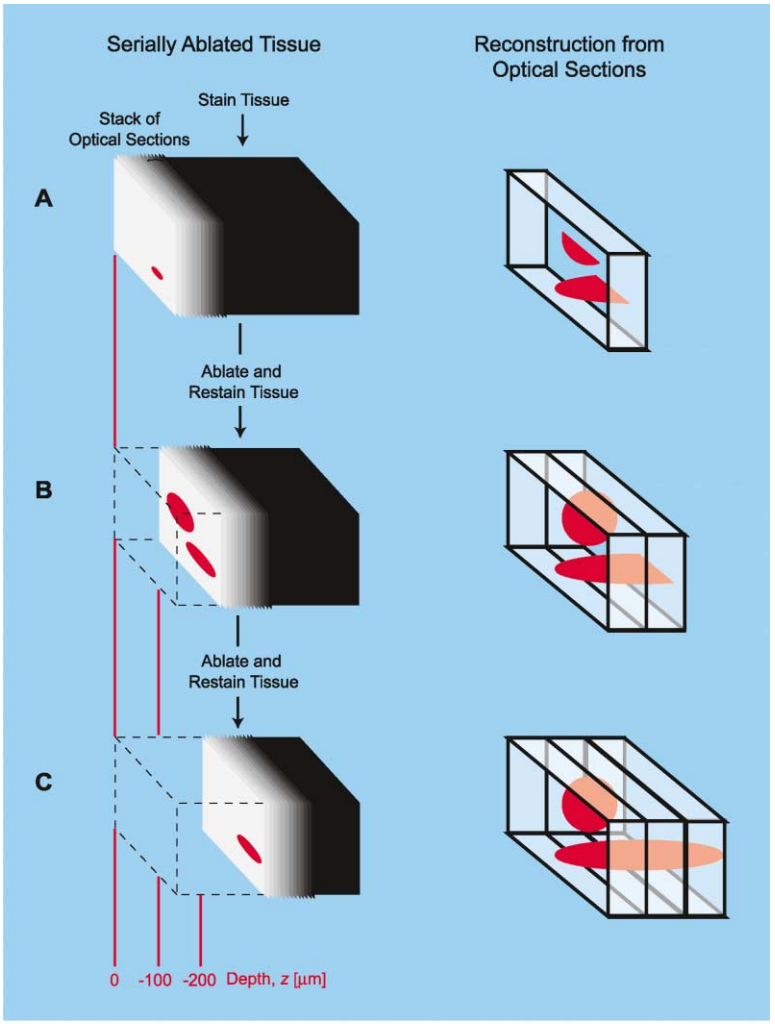

Figure 1. The Iterative Process by which Tissue Is Imaged and Cut in All-Optical Histology

(A) A tissue sample (left column) containing two fluorescently labeled structures is imaged by conventional two-photon laser scanning microscopy to collect optical sections through the ablated surface. Sections are collected until scattering of the incident light reduces the signal-to-noise ratio below a useful value; typically this occurs at ~150 μm in fixed tissue. Labeled features in the resulting stack of optical sections are digitally reconstructed (right column).

(B) The top of the now-imaged region of the tissue is cut away with amplified ultrashort laser pulses to expose a new surface for imaging. The sample is again imaged down to a maximal depth, and the new optical sections are added to the previously stored stack.

(C) The process of ablation and imaging is again repeated so that the structures of interest can be fully sectioned and reconstructed.

of unamplified pulses to image tissue could be envisioned to permit iterative ablation and imaging of a tissue preparation (Figure 1).

A priori, it is unclear if the ablations performed with amplified ultrashort laser pulses will produce concurrent secondary damage that would render the faced-off block of tissue unusable for imaging with TPLSM. For example, a loss of image resolution could result from photo-induced damage to proteins in the tissue adjacent to the ablated surface, sufficiently high levels of photo-induced autofluorescence in the adjacent tissue, or cavitation of the ablated surface to create craters that extend the full imaging depth of TPLSM. The present study addresses these issues and advances the development of an all-optical histology. We test if laser ablation methods preserve optical properties so that TPLSM may be used for imaging intrinsic and applied fluorescent probes, and if these images may be used to reconstruct three-dimensional architectonics in a region of the brain.

Realization

The all-optical histology technique makes use of successive iterations of imaging with TPLSM and ablation with ultrashort pulses of infrared laser light to provide diffraction-limited volumetric data that is used to reconstruct the architectonics of labeled cells or microvasculature. The surface layers of the tissue are stained, if necessary, and then imaged using TPLSM (Figure 1). The region of the tissue that has been imaged is subsequently removed by laser ablation with amplified ultrashort laser pulses. The newly exposed surface is then restained, if necessary, then imaged, and then ablated. The sequence repeats serially until the desired volume of tissue has been analyzed. This leads to a digitized block of optical sections from the labeled tissue that reveals features within the block of tissue (Figure 1). The ability to maintain the physical location of a sample, and the ability to use samples in the unfrozen state, suggests the utility of this path to automate histological analysis.

In our realization, the tissue to be processed is positioned on an automated X-Y translation table that can be moved in a raster pattern across the focus of the amplified laser beam. To facilitate milling the smoothest possible cuts, we direct the laser typically through a water immersion objective with a numerical aperture (NA) in the range from 0.2 to 0.7 NA. Objectives with a lower NA promote white-light generation, which will degrade the fidelity of the laser pulse (Ashcom et al.,

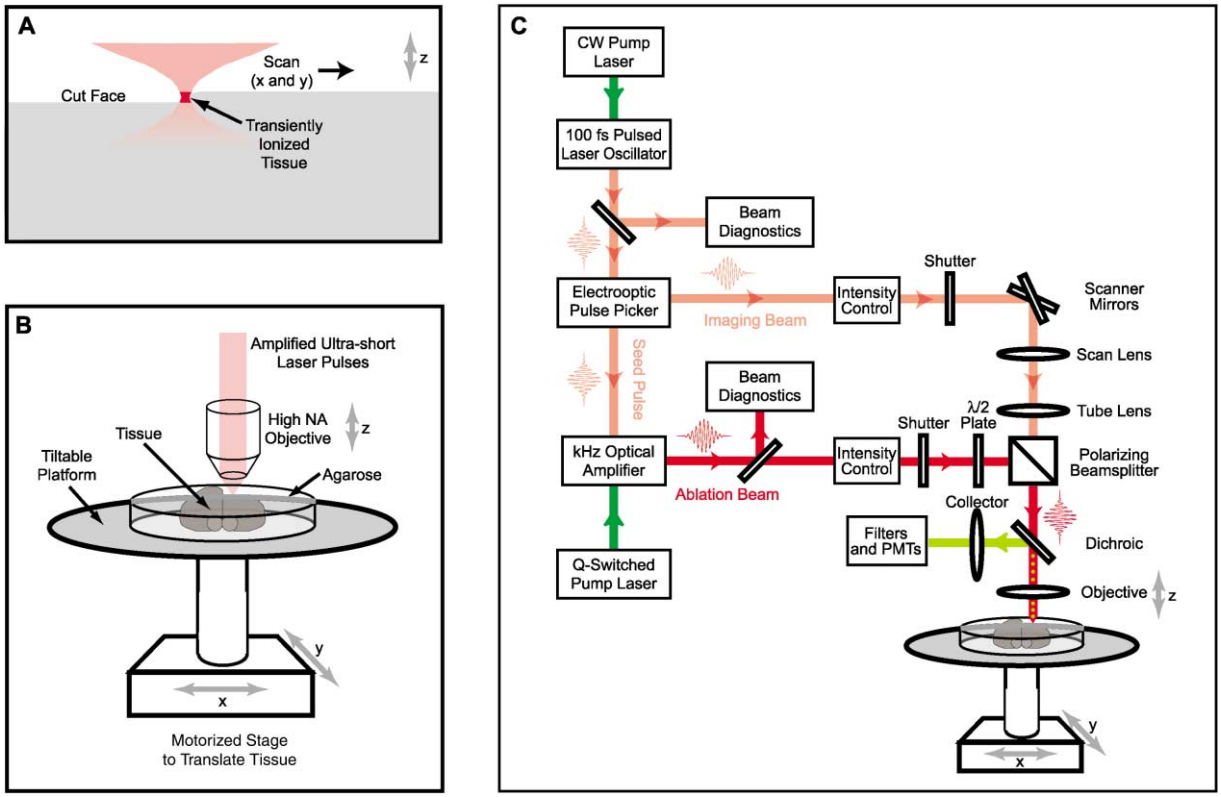

Figure 2. Schematic of the Mechanical and Optical Aspects of the Amplified Ultrashort Laser Ablation and Subsequent TPLSM Imaging

(A) Cutting is performed with high-energy pulses, i.e., typically 1 to 10 μJ, and high numerical aperture objectives, i.e., typically 0.2 to 0.7 NA, to ablate small volumes, i.e., typically 10 to 100 femtoliter, with relatively high precision. The focus region is in red; this region approximately corresponds to the ablation volume at the threshold energy for ablation.

(B) Configuration of the tissue and tissue platform for cutting with a high NA objective. The focus of the laser beam is adjusted by changing the height (axial dimension) of the objective, and the tissue is ablated by smoothly moving the tissue platform in a raster pattern (lateral dimensions) through the use of computer-controlled stepping motors.

(C) Schematic of major optical components. The laser oscillator is Titanium:Sapphire with a pulse width of ~120 fs that is used both as the source for the two-photon microscope and as a seed for a multipass optical amplifier. The pump lasers are a continuous wave (CW) solid-state laser for the oscillator and a pulsed solid-state laser for the amplifier. The beam diagnostics include a power meter, spectrometer, and autocorrelator. Only the major illumination optics for TPLSM, including the scanners, scan lens, tube lens, and objective lens, and the major detection optics for TPLSM, including the dichroic mirror, collector lens, and photomultiplier tube, are shown. The polarization optics and polarizing beam splitter cube serve to overlay the paths of the imaging and ablation beams. Lastly, laser timing circuitry for the amplifier as well as the computer control for the two-photon microscope and associated data acquisition are not shown. See Experimental Procedures for details.

2002). The choice of the numerical aperture is further based on considerations that tie the NA of the microscope objective to the ablated volume (see Appendix). The beam is focused at the surface of the tissue or just deep to the surface (Figure 2A). The tissue is mounted on a goniometer to allow leveling and alignment of the tissue surface relative to the optical axis that is defined by the objective. A motorized stage allows movement of the preparation to effect continuous tissue removal (Figure 2B). For the optimization studies described below, the tissue was typically ablated with a raster scan pattern to remove thin layers, typically 5 to 20 μm, after which the objective was lowered relative to the sample and an additional layer was ablated.

A single apparatus encompasses the ablation and TPLSM imaging optics (Figure 2C). Ablation is accomplished with amplified laser light that uses an amplifier of local design and seed pulses that are picked off from the imaging beam. The ablation and imaging beams are tagged with orthogonal polarizations and mixed with a polarizing beam splitter between the tube lens and objective. The foci of these beams are aligned to coincide. We ablated at a fixed center wavelength (λ) of $\lambda \approx$ 800 nm while we imaged at wavelengths that selectively highlighted different features in the tissue.

Results

Ablation Parameters

We use a succession of point ablations to remove channels and planes of brain tissue. There are three parameters that may be optimized for the ablation process. The first is the fluence. This is set by the energy per pulse and the choice of NA for the objective. The second is the rate of scanning. This is set by the speed of the translation of the tissue and the repetition rate of the optical amplifier, which changes the number of pulses delivered to a voxel in the tissue. The third is the axial

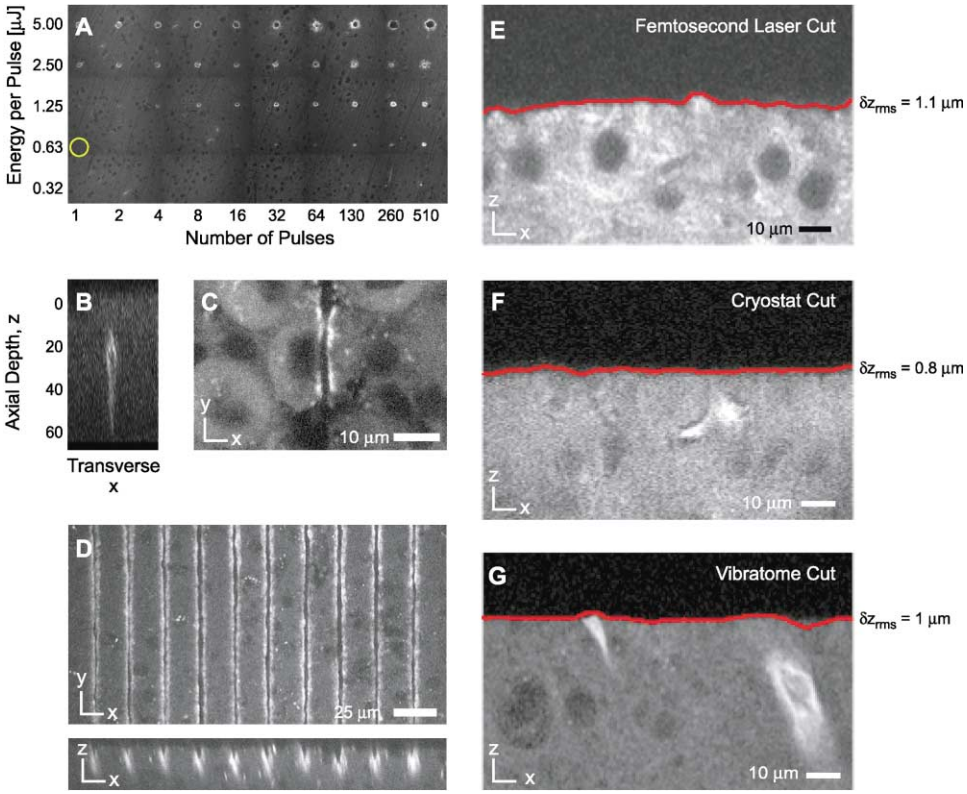

Figure 3. Threshold and Fine-Scale Tissue Cutting and Associated Surface Roughness

(A) Array of ablation craters, in fixed neocortical tissue from rat, as a function of the energy per pulse (vertical axis) and number of laser pulses (horizontal axis). Ablation was performed with a 10× magnification, 0.2 NA air objective. The distance between craters is 100 μm. The image is a single section obtained with TPLSM at $\lambda = 760$ nm to highlight intrinsic fluorescence. The yellow circle highlights the lowest energy at this NA for clearly observed ablation in a single pulse.

(B) Transverse maximal projection through the ablation volume created by a single pulse at an energy of 0.65 μJ. The sections were obtained as for (A). Note the intrinsic fluorescence that surrounds the ablated dark, inner region.

(C) A line cut in fixed cerebellar tissue from a CFP-transgenic mouse to further demonstrate the precision of the cutting process. The laser was focused onto the preparation with a 10× magnification, 0.3 NA air objective, and four passes, at a scan rate of 0.1 mm/s, were made to cut each line. The energy per pulse was 2.0 μJ. The optical sections were obtained with TPLSM at $\lambda = 850$ nm and the image corresponds to maximal projections through a depth of 3 μm.

(D) Lines cut in fixed neocortical tissue from mouse to demonstrate the reproducability of the cutting process with ultrashort laser pulses. The laser was focused onto the preparation with a 10× magnification, 0.3 NA air objective, and two passes, at a scan rate of 0.1 mm/s, were made to cut each line. The energy per pulse was 0.5 μJ. The optical sections were obtained with TPLSM at $\lambda = 750$ nm to highlight intrinsic fluorescence; the top view corresponds to a maximal projection through a depth of 20 μm at and just below the surface, while the side view is a maximal projection over a lateral distance of 3 μm.

(E) Detail of the cut surface for fixed cortex from mouse cut with pulsed laser light. The laser was focused onto the cut face with a 20× magnification, 0.5 NA water objective, and single passes, at scan rates of 2 to 4 mm/s, were made to optically ablate successive planes at a depth of 10 μm each. The energy per pulse was 7.5 μJ. The samples were stained with 5-hexadecanoylamino-fluorescein and imaged with TPLSM at $\lambda = 800$ nm. The root-mean-square variation of the surface across a 100 μm by 100 μm area is indicated in the following panels.

(F) Detail of the cut surface for fixed and frozen neocortex from mouse that was cut with a cryostat.

(G) Detail of the cut surface for fixed neocortex from mouse that was cut with a Vibratome™.

step size between ablated layers. The evaluation of these cutting parameters relies primarily on TPLSM imaging of the cut block face at a range of magnifications.

Point Ablations

To establish the relationship between the energy of the pulses and the spatial extent of the point ablations, we systematically varied both the energy per pulse and the number of pulses to generate an array of ablation sites in fixed neocortex from rat. The ablations took the form of small craters of graded sizes with the largest holes made by 510 consecutive 5 μJ pulses (Figure 3A). The bright border surrounding each hole stems from an increase in autofluorescence that accompanies the laser cutting. This autofluorescence is enhanced by illumination of the preparation near $\lambda \approx 750$ nm (Xu et al., 1996).

We observed formation of a crater at a minimum energy of 0.63 μJ for a single pulse application with this array (Figures 3A and 3B), which corresponds to a fluence of $F_T \sim 3$ J/cm^2 at the focus for the parameters of our beam at the threshold for ablation. The ablation volume has a greater depth along the *z* axis than width along the *x* and *y* axes (Figure 3B), consistent with a simple model (see Appendix). Further, an increased number of laser pulses only weakly compensates for lower pulse energies, i.e., by approximately 2-fold for 130 pulses (Figure 3A). Thus, cutting is most efficient,

in terms of total energy expenditure, with one or few pulses whose fluence lies above the threshold value. This implies that the scan rate should be chosen to insure approximately one area of ablation per pulse. For a 0.2 NA lens and the 1.2 kHz repetition rate of our amplifier (Experimental Procedures), the maximum scan rate is limited to approximately 5 mm/s. Of interest, the threshold value of the fluence is in agreement with the value of the threshold for laser ablation of bovine brain tissue that was freshly dissected (Loesel et al., 1998) as well as for laser ablation of various glasses (Stuart et al., 1996).

Line or Channel Ablations

We next tested the fidelity with which lines could be cut when fixed brain tissue is translated across a beam that is focused at the surface of the tissue. The scale of these fine cuts is on the order of 2 μm in diameter, as observed in cuts through Purkinje cell somata and nuclei that were endogenously labeled with cyan-emitting fluorescent protein (CFP) and imaged at $\lambda = 850$ nm (Figure 3C). The reproducibility of both the diameter and depth of these cuts is illustrated by a parallel array of ten channels cut in fixed neocortical tissue (Figure 3D, top). The corresponding troughs to each channel measure approximately 6 μm to their deepest point (Figure 3D, bottom). This sets the scale for the finest cuts that can be made and also establishes the capacity to make reproducible long channels in brain tissue.

Surface Roughness

The roughness of the ablated surface formed by the removal of a plane of brain tissue was evaluated in order to determine if TPLSM would be an effective imaging tool with tissue that was prepared with ultrashort laser pulses. In particular, a sufficiently great roughness would detract from the advantages of TPLSM imaging. Large channels, several hundred microns in width, were ablated into fixed neocortex from mouse using an axial step size, i.e., z step, of 10 μm and, as a conservative measure, relatively high fluence. The surface of the ablated channel was stained with 5-hexadecanoylamino-fluorescein, a lipid soluble dye. Subsequently, the tissue was mechanically cut along a plane perpendicular to the length of the ablated channel. A short strip along the ablated surface was imaged at a wavelength of $\lambda = 800$ nm and the variations in height were analyzed to quantify the roughness of the surface (Figure 3E). We estimated the root-mean-square (RMS) deviation of the ablated surface to be (n = 40 sections; see Experimental Procedures):

$$\delta z_{RMS}^{\text{ultrashort pulses}} = 1.1 \pm 0.1 \ \mu\text{m (mean} \pm \text{SEM)}.$$

For comparison, similarly fixed neocortical tissue from mouse was equilibrated in 30% (w/v) sucrose, rapidly frozen, and cut with a cryostat (Figure 3F). An analysis of the surface roughness of a block face from which 10 μm sections had been cut yielded

$$\delta z_{RMS}^{\text{cryostat}} = 0.8 \pm 0.1 \ \mu\text{m}.$$

A final comparison was made with similarly fixed but unfrozen tissue blocks that were faced off with a Vibratome™ (Figure 3G). Here, the surface exhibited some large-scale variations, but on the fine scale of 1 to 100 μm, the local roughness was $\delta z_{RMS}^{\text{vibratome}} \approx 1$ μm. Thus, the roughness of the optically ablated surface is similar to that of surfaces that are cut frozen or unfrozen with traditional knives. We further conclude that the roughness of a block face that is trimmed with amplified ultrashort laser pulses is well within the depth of imaging with TPLSM, so that the two methods are compatible.

Large-Scale Volume Ablation

Although the extent of collateral heating is believed to be negligible for ablations with ultrashort laser pulses (Loesel et al., 1998), it was important to test if scaling up the volume of ablations in brain tissue preserves the imaging properties of the preparation. We considered the ablation of millimeter-sized slabs in fixed neocortical tissue from rat (Figure 4A), for which we chose an axial step size of 20 μm. Sets of five consecutive ablation scans were performed to remove a slab of approximately 100 μm in total thickness. This process was repeated three times to form a staircase pattern of remaining tissue. We observed that ablated tissue was readily cleared by the saline buffer, so that debris did not accumulate or stick to the cut surfaces. At the macroscopic level, the cut surfaces appeared flat, with sharply defined walls. A side view of similar cuts was obtained in tissue that was en block stained, after ablation, with 5-hexadecanoylamino-fluorescein (Figure 4B). The edges of these cuts appear smooth.

As a further test of the ability for laser ablation to reliably remove tissue from unfrozen brains, we tested these methods with embryonic mouse brain. This tissue is particularly difficult to section with traditional techniques, largely because of the low content of glia and connective tissue and the high content of fluid. Yet such tissue, with its relatively high transmission of light, appears to be ideally suited for the all-optical histology technique. We thus considered the large-scale ablation and imaging of perfused and fixed mouse embryos as early in development as E15. The embryos were mounted in agarose with the lateral surface of the head exposed. Multiple ablation passes at increasing axial depth were performed until over 800 μm of tissue depth was removed (Figure 4C). Despite the fragility of unfrozen embryonic brain tissue, the gross structure of the brain and lateral ventricle appeared normal after large-scale laser tissue removal.

Test of Photo-Damage

Our strongest concern in the use of ultrashort laser pulses for histology was the retention of normal tissue properties in the adjacent, unablated regions. We evaluated the collateral damage in the tissue immediately adjacent to the ablation with four metrics: (1) preservation of physical integrity of the cell surface and cell organelles as assessed by application of fluorescent probes; (2) preservation of antigenic response as assessed by immunostaining adrenergic projection systems in the neocortex; (3) the induction of increased autofluorescence in cortical tissue; and (4) the retention of fluorescence in tissue from transgenic animals that expressed fluorescent proteins.

To test for integrity of cell surface membranes, laser-

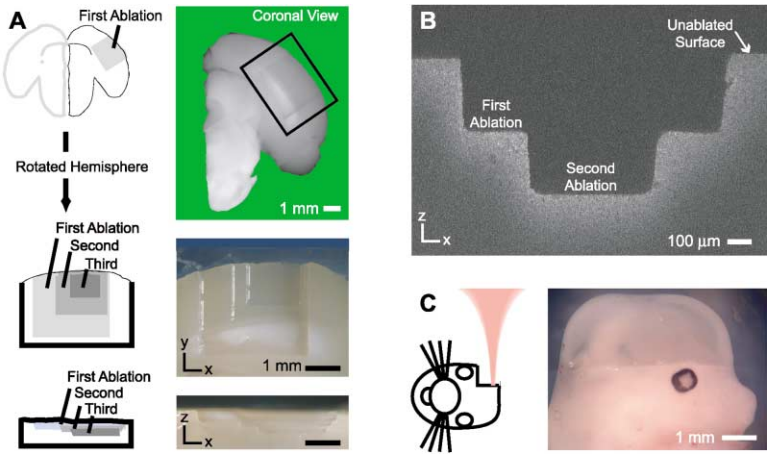

Figure 4. Demonstration of Large-Scale Tissue Cutting in Adult and Embryonic Tissue

(A) Macroscopic images and accompanying cartoons of three successive ablations in fixed cortical tissue from rat. A coronal section in the posterior part of one hemisphere was prepared with a mounted knife. The laser was focused onto the cut face with a 10× magnification, 0.2 NA air objective. Single passes, at a line-scan rate of 1.5 mm/s, were made to optically ablate successive planes at a depth of 20 μm each. The first cut removed a 3 mm by 3 mm square to a depth of 250 μm into the tissue. This was followed by a second cut to remove a 2 mm by 2 mm square to a depth of 350 μm and a third cut to remove a 1.5 mm by 1.5 mm square to a final depth of 470 μm. The energy per pulse was 33 μJ. The images were obtained with bright-field microscopy.

(B) Side view of a double channel cut into fixed cortical tissue from mouse, prepared as in (A). The laser was focused onto the cut face with a 20× magnification, 0.5 NA water objective, and single passes, at scan rates of 2 to 4 mm/s, were made to optically ablate successive planes at a depth of 10 μm each. The first cut removed a 1 mm by 1 mm square to a depth of 200 μm, while the second removed a 0.5 mm by 0.5 mm square to a final depth of 360 μm. The energy per pulse was 7.5 μJ. The cut squares were stained with 5-hexadecanoylamino-fluorescein, then bisected with a knife and imaged on edge with TPLSM at $\lambda = 800$ nm.

(C) Macroscopic images and accompanying cartoon of the head of an E15 embryo after a two-step ablation sequence. The laser was first focused onto the tissue with a 10× magnification, 0.3 NA water objective, and single passes, at a scan rates of 4.0 mm/s, were made to optically ablate successive planes at a depth of 50 μm each for a total depth of 550 μm below the original surface; the energy per pulse was 23 μJ. The laser was then focused onto the tissue with a 20× magnification, 0.5 NA water objective, and single passes at the same scan rate ablated successive planes at a depth of 10 μm each for an additional depth of 250 μm; the energy per pulse was 24 μJ. Skin, bone, and vasculature, as well as neuronal tissue, were cut.

ablated embryonic tissue was stained by the surface application of 5-hexadecanoylamino-fluorescein and imaged with TPLSM along the same axis as used for the ablation (Figures 5A–5C). Under low magnification, we observed that there was no distortion of the brain topology, despite the prominent size of lateral ventricles in embryos (Figure 5A). Examination at higher magnification shows that a multitude of tissue types, including skin, bone, and brain, have been cleanly cut (Figure 5B). High-resolution images of the ventricular zone in the lipid-stained material reveals chains of neurons whose orientation and shape are consistent with those from preparations of embryonic mouse cortex that have been frozen or hardened in embedding media for conventional histological sectioning (Figure 5C; Levitt et al., 1981; Rakic, 1972; Takahashi et al., 1995).

The application of acridine orange to laser-ablated mouse cortex, imaged at $\lambda = 800$ nm, was observed to stain nucleic acids in both cell cytoplasm and nucleus (Figures 5D–5F). High-resolution images of the ventricular zone show examples of condensed chromosomes and dividing cells with clear metaphase plates in evidence (asterisk in Figure 5F). These features are consistent with the known cell division that takes place at the base of the ventricular zone in mammalian cortex during its neurogenesis (Takahashi et al., 1995). These data demonstrate that all-optical histology is a tool to ablate and image the embryonic brain with diffraction-limited spatial resolution, as collateral damage from the ablation process does not markedly distort brain structure down to the level of chromosomes.

Assay for Immunoreactivity

Given the labile nature of protein, it was important to test if optical histology is compatible with preservation of protein antigenic reactivity and immunolocalization. A measure of possible collateral damage was the antigenic response of tissue for tyrosine hydroxylase (TH), an enzyme that is required for the synthesis of monoamine neurotransmitters such as dopamine and noradrenaline. In the telencephalon, TH-containing fibers form scattered and diffuse plexi of thin axons (Cooper et al., 1996). We examined the survival of TH immunoreactivity immediately adjacent to an ablated surface after a channel was cut with amplified ultrashort laser pulses whose fluence was well above threshold, as in Figure 4B. The brain was then equilibrated with sucrose to allow for sectioning on a freezing-sliding microtome in a plane that was oriented perpendicular to the ablated surface. Free-floating sections were then stained with antibodies for TH, which were visualized as a dark reaction product. At low magnification, the dense immunostaining persists without decrement near the ablation surface (Figure 5G). Furthermore, the TH fibers that course dorsal to the corpus callosum could be seen, at high magnification, to extend out into the edge of the laser-ablated brain tissue with tissue from rodents that were either perfusion fixed (Figure 5H) or exsanguinated without fixation (Figure 5I). Note that the surface of the brain that was not laser ablated has a similar appearance to that of the laser-ablated cut surface (Figure 5G). This post hoc analysis shows that antigenicity and therefore protein conformation, at least for the TH antigen, is retained in tissue after laser ablation.

Endogenous Fluorescence and Wavelength Selection

We consider the possibility of laser-induced increase in autofluorescence, as this could limit the detection of fluorescent labels from endogenous fluorophores in transgenic animals. Specifically, we used animals that

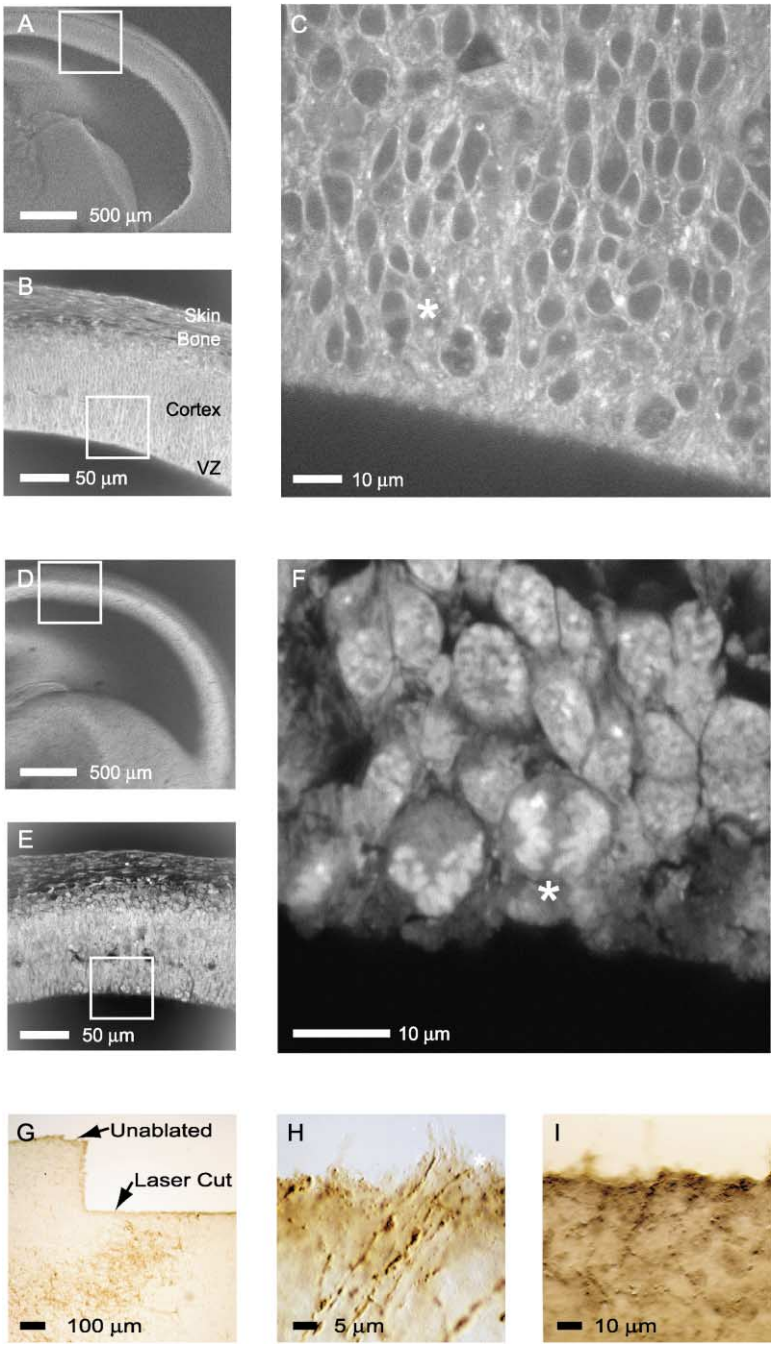

Figure 5. Preservation of Cellular Integrity as Assayed with Labels of Subcellular Structures

(A–C) Images from the head of an E15 embryo, in which the laser was focused onto the tissue with a 20× magnification, 0.5 NA water objective, and single passes at a scan rate of 4.0 mm/s were used to ablate successive planes at a depth of 10 μm; the energy per pulse was 24 μJ. The cut surface of the tissue was stained with the fluorescent lipid analog 5-hexadecanoylamino-fluorescein, and optical sections were taken with TPLSM at λ = 800 nm. The successive panels show single sections with increasing magnification, as outlined by the white boxes. Note that the cell somata are unstained (C). The asterisk points to a cell in the ventricular zone (C) that has recently undergone division.

(D–F) Tissue from a second embryonic mouse, prepared identically to that in (A) to (C), was stained with the water-soluble nucleic acid dye acridine orange and optical sections were taken with TPLSM at λ = 800 nm. The successive panels show single sections with increasing magnifications. The asterisk points to a cell in the ventricular zone (F) that is undergoing division.

(G) Immunoreactivity near an optically cut surface in fixed neuronal tissue. The laser was focused onto the cut face of the tissue with a 20× magnification, 0.5 NA water objective, and single passes, at a line-scan rate of 4.0 mm/s, were made to optically ablate successive planes at a depth of 10 μm each. The channel had a final depth of 370 μm. The energy per pulse was 2.2 μJ. After completion of the optical cutting, the tissue was frozen, physically sectioned on a sliding microtome at a thickness of 25 μm, immunostained with anti-tyrosine hydroxylase, and visualized with DAB. The tissue was imaged under bright-field microscopy. The brown regions correspond to immunostained axons and cell bodies.

(H) Tissue prepared and stained similarly to that in (G) but imaged at high magnification under Nomarski optics to illustrate the cutting of individual axons (*).

(I) Immunoreactivity near an optically cut surface in fresh neuronal tissue. Conditions for cutting were the same as in (G), except that the tissue was cut at a scan rate of 2.0 mm/s and the energy per pulse was 23.3 μJ. Note the dark reaction product close to the cut surface.

expressed yellow cameleon 3.0, a fusion protein that contains cyan-emitting fluorescent protein (CFP) as one constituent, in the walls of the cortical vasculature (Experimental Procedures). Our sample consisted of fixed tissue from neocortex of the transgenic animals in which a 100 μm wide channel was ablated. The direction of the imaging beam paralleled that used for the ablation; we present maximum projections normal to the beam path in order to assess the induction of autofluorescence near the ablated surface. When imaged at λ = 750 nm, a relatively high level of autofluorescence is seen in tissue that lies within 20 μm of the ablated surface (Figure 6A). When imaged at λ = 850 nm, labeled vasculature can be visualized down to a depth of approximately 150 μm below the ablated surface (Figure 6B). Thus, the increase in autofluorescence close to the ablated surface does not impede imaging deep into the tissue since this potential problem is circumvented by imaging with wavelengths of 850 nm or longer.

The observation of significant autofluorescence near $\lambda \approx$ 750 nm is consistent with the increased short-wavelength absorption by molecules such as nicotinamide adenine dinucleotide (NADH) (Figure 6C). As shown above (Figures 6A and 6B), absorption by this and other molecules that are involved in cell energetics (Xu et al., 1996) may be circumvented by imaging at longer

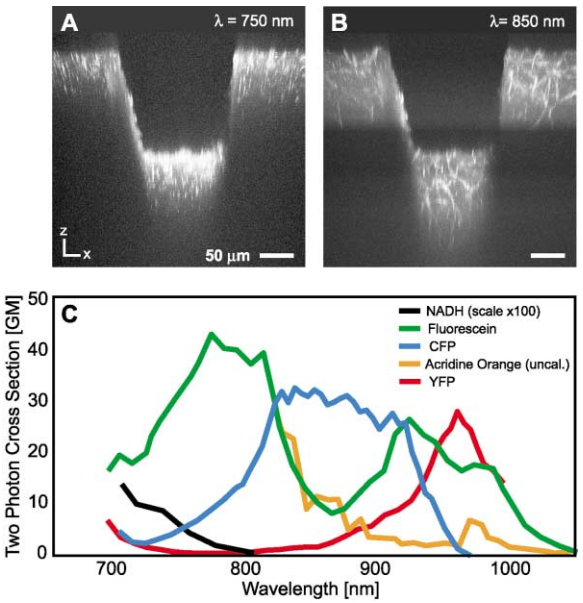

Figure 6. Wavelength Selection for Imaging into Ablated Tissue

The laser was focused onto the cut face of fixed cortical tissue from a CFP-transgenic mouse with a 20× magnification, 0.5 NA water objective, and single passes, at a line-scan rate of 4.0 mm/s, were made to optically ablate successive planes at a depth of 10 μm each. The channel had a final depth of 170 μm. The energy per pulse was 2.2 μJ.

(A) The optical sections were obtained with TPLSM at $\lambda = 750$ nm. This wavelength excites a high level of background autofluorescence.

(B) The sections obtained with the longer wavelength, $\lambda = 850$ nm, which excites the CFP label and a much lower level of autofluorescence. The labeled vasculature is now apparent.

(C) Two-photon action spectra of selected fluorophores that are relevant for the imaging of brain tissue. The spectrum for NADH contributes to tissue autofluorescence (Xu et al., 1996), the spectrum for fluorescein corresponds to that for the lipid analog 5-hexadecanoylamino-fluorescein (Xu and Webb, 1996), the spectrum for acridine orange bound to DNA corresponds to the nucleic acid stain (Bestvater et al., 2002) and has uncalibrated units, and the spectra for CFP and YFP correspond to labels in the transgenic mice (Tsai et al., 2002).

wavelengths. This suggests the utility of cell-specific labeling with the endogenous fluorescent proteins CFP, for which the two-photon absorption has a broad peak between $\lambda \approx 820$ and 880 nm, and yellow-emitting fluorescent protein (YFP), for which the two-photon absorption peaks near $\lambda \approx 950$ nm (Figure 6C). Practical considerations, which include the decrease in power from the Ti:Sapphire laser oscillator at long wavelengths and the decreased transmission of common objectives at long wavelengths, suggested the utility of an excitation wavelength of $\lambda \approx 920$ nm for YFP in our apparatus.

Iterative Volumetric Reconstruction

We now turn, by means of two examples, to the core issue of three-dimensional reconstructions of labeled tissue (Figure 1). In the first example, we performed serial ablation and imaging of the fixed neocortex of transgenic mice in which infragranular projection neurons selectively expressed YFP (Feng et al., 2000). Optical imaging and ablation was performed in the radial direction over a lateral extent of 200 μm. Each iteration of imaging comprised a total depth of approximately 110 μm, of which 60 μm represented new information and 50 μm represented overlap with prior images as a means to cross-check alignment. The image stacks are displayed as a maximal projection in the coronal direction (Figure 7A). The stacks from 24 iterations of cutting and imaging were overlaid and merged to generate a three-dimensional matrix of intensity values that extend the full depth of neocortex (Figure 7A). The maximal projection of this matrix allows visualization of fine structures, which are highlighted with the contrast inverted (Figure 7B) and compares favorably with the published coronal images (cf. Figure 7B with Figure 7E of Feng et al., 2000).

Next, to demonstrate the volumetric reconstruction of extended microscopic structures, we performed serial ablation and imaging of the fixed neocortex of CFP transgenic mice in which the neocortical vasculature in a medial region of parietal cortex expresses CFP (Figures 8A–8D). Each stack of images comprised a total thickness of approximately 200 μm, and stacks from four iterations of cutting and imaging were overlaid to generate a three-dimensional matrix of intensity values. The raw image data was band-pass filtered and processed with standard imaging processing routines to extract the edges of the walls (Experimental Procedures). This process defines a reconstructed volume of the underlying vasculature that can be rendered by ray-casting and rotated for optimal viewing (Figure 8E). The tortuous architecture of the vasculature is similar to that seen with latex casts (Harrison et al., 2002; Motti et al., 1986). Further, the volume of the vasculature can be quantified from the reconstruction. For this data set (Figure 8), we estimate that the volume fraction of the vasculature relative to the rest of the brain is 6% ± 1%. This valve includes the vessel lumen and walls.

Discussion

We have demonstrated the use of amplified ultrashort laser pulses with fluences from approximately 6 to 600 J/cm^2 to precisely ablate fresh and fixed neuronal tissue from adult (Figures 3–8) and embryonic (Figures 4 and 5) animals. In combination with established labeling procedures (Figure 1), two-photon laser scanning microscopy (Figure 2), and volumetric reconstruction techniques (Figure 9), the ablation process comprises a set of tools required for the all-optical analysis, reconstruction, and quantification of neuronal (Figure 7) and vascular structures (Figure 8). The use of laser light to perform both physical sectioning and optical imaging constitutes a novel methodology that obviates the need to freeze or embed tissue and register cut sections, and thus is conducive to the complete automation of histology. Of particular importance, the ability to readily and reliably process embryonic tissue is critical for the study of genetic mutations that produce nonviable animals.

The present work shares elements with two recent technologies in neuroanatomy. The first is the demonstration of successive cutting and imaging as a means to form atlases of the human brain (Rauschning, 1986; Toga et al., 1994). In this procedure, the entire head is

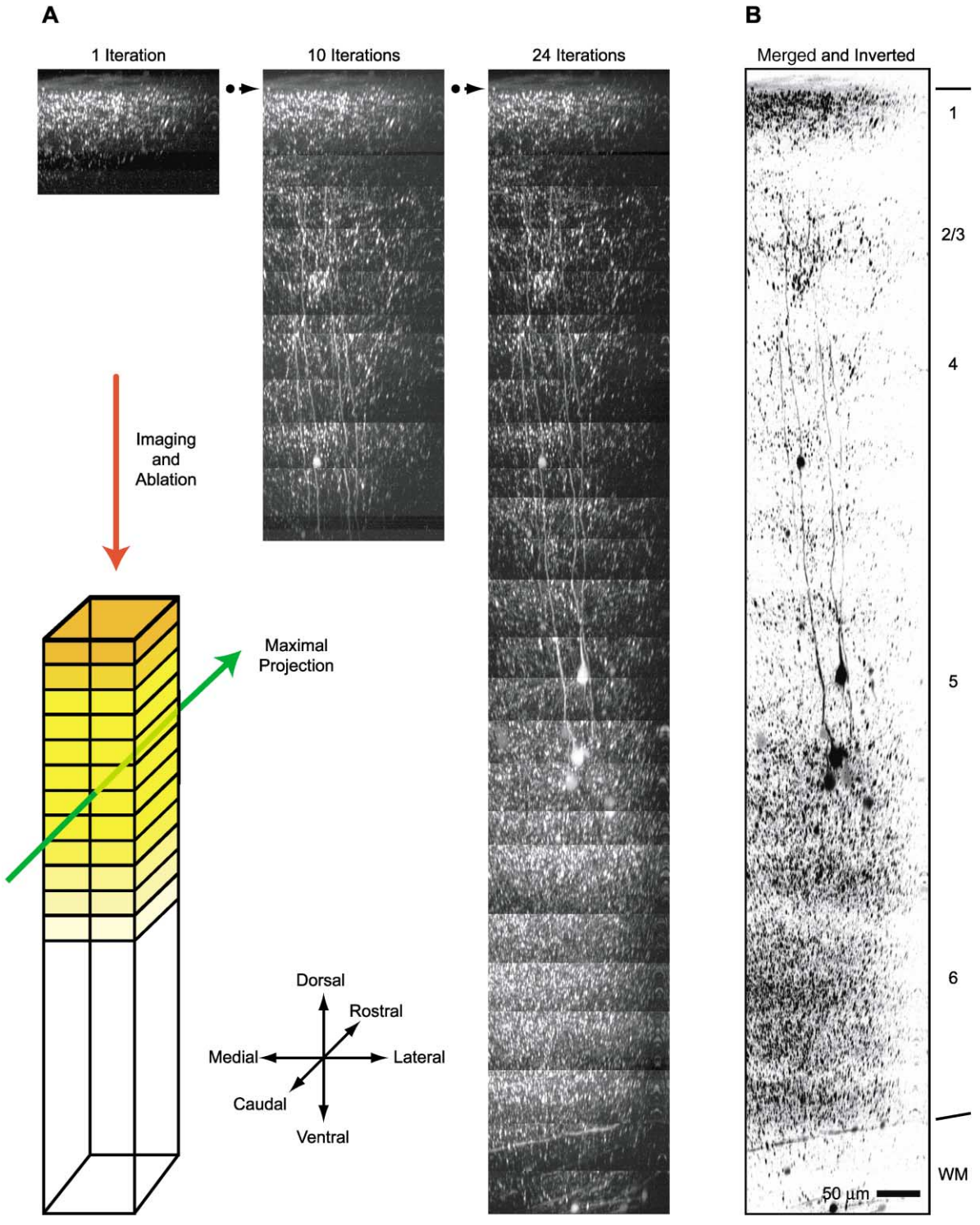

Figure 7. Optical Cutting, Optical Sectioning, and Maximal Projection to Show Labeled Neurons in Neocortex in Mouse Neocortical Tissue

(A) Iterative processing of a block of neocortex of a YFP labeled transgenic mouse. Twenty-four successive cutting and imaging cycles are shown. The laser was focused onto the cut face with a 20× magnification, 0.5 NA water objective, and single passes, at a scan rate of 4 mm/s, were made to optically ablate successive planes at a depth of 10 μm each with total thicknesses between 40 and 70 μm per cut. The energy per pulse was maintained at 8 μJ. Each stack of images represents a maximal side projection of all accumulated optical sections obtained using TPLSM at $\lambda = 920$ nm. The sharp breaks in the images shown in successive panels demarcate the cut boundaries.

(B) Maximal side projection through the complete stack with the breaks removed by smoothly merging overlapped regions. The contrast is inverted to emphasize the fine labeling.

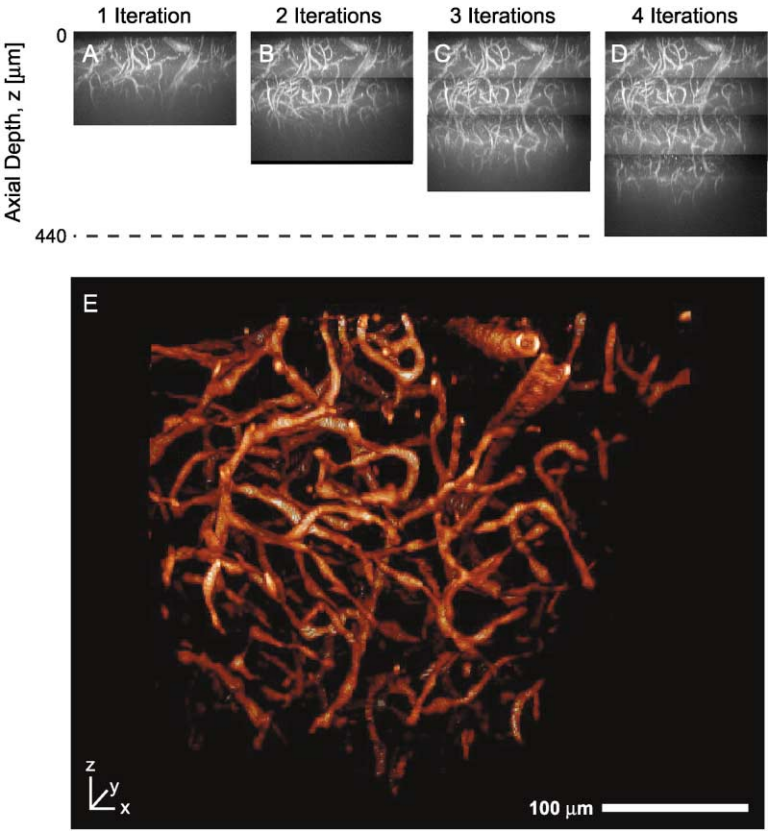

Figure 8. Optical Cutting, Optical Sectioning, and Volumetric Reconstruction of Labeled Vasculature in Mouse Neocortical Tissue

(A–D) Serial reconstruction of vasculature in a block of neocortex of a CFP-labeled transgenic mouse. Four successive cutting and imaging cycles are shown. The laser was focused onto the cut face with a 20× magnification, 0.5 NA water objective, and single passes, at a scan rate of 0.5 mm/s, were made to optically ablate successive planes at a depth of 10 μm each with total thicknesses of 70 μm per cut. The energy per pulse varied from 0.4 to 1.7 μJ. Each stack of images in (A) through (D) represents a maximal side projection of all accumulated optical sections obtained using TPLSM at $\lambda = 850$ nm. The sharp breaks in the images shown in successive panels demarcate the cut boundaries.

(E) A volume rendering of the vasculature at the same azimuthal angle but rotated by 44° along their vertical axis. The raw data in (D) was processed by the numerical algorithm illustrated in Figure 9.

frozen and a heavy blade is used to section through bone and soft tissue. The newly cut surface is imaged under reflected light; the contrast between different brain regions originates from differences in the distribution of cell sizes and myelination. While the resolution is limited, i.e., typically $100 \times 100 \times 50$ μm^3 voxels are recorded, it exceeds that of magnetic resonance imaging (Toga et al., 1997). By comparison with the present technique, frozen tissue has limited optical penetration depth, so that only sections directly at a cut surface may be recorded. Further, the surface may contain microscopic defects formed by the action of the blade. By comparison, all-optical histology permits diffraction-limited images to be obtained throughout the entire extent of the brain, i.e., approximately $V_{focus} = 0.5 \times 0.5 \times 1.0$ μm^3 voxels, albeit at the cost of more complex machinery.

A second related technology in neuroanatomy is the microdissection of small regions of tissue, or even single cells, with laser light (Eltoum et al., 2002). These methods are being rapidly adopted as a means to identify gene expression patterns on the cellular level by application of, for example, reverse transcriptase polymerase chain reaction (RTPCR) methods on small numbers of cells that are identified and selectively laser microdissected from previously sectioned and stained tissues. The all-optical histology methods may offer a complementary approach to laser microdissection methods, in that the tissue of interest could be left intact as the surrounding tissue is removed in a preparation that would not have been previously conventionally sectioned and slide-mounted.

Tissue Fidelity

We observed that cutting with microjoule laser pulses led to clean cuts of axons (Figure 5H). There was an overall root-mean-square surface roughness of approximately 1 μm (Figure 3E), which is close to that obtained with frozen tissue cut in a cryostat (Figure 3F). Further, despite potential photo-bleaching and photo-damage by the high-intensity laser pulses, i.e., $\sim 10^{14}$ W/cm^2 at the focus, both antigenic recognition (Figures 5G–5I) and the fluorescence of endogenous fluorescent proteins (Figures 6B, 7, and 8A–8D) were retained by the tissue to within 10 μm of the ablated region. Additionally, both stain penetration and imaging through the ablated surface were resilient to the ablation process.

The relative lack of photo-damage may be understood in terms of the low duty cycle of the amplified laser light source and the relatively small number of quanta absorbed outside the ablated volume. A calculation similar to that used to determine the volume ablated on each pulse (see Appendix) suggests that the absorption of fluorophores only within 10 to 30 microns of the ablated region is saturated by the laser pulse. Given that the pulse width of 100 fs is far less than a typical excited-state lifetime of 1 ns, fluorophores near the cut are likely to absorb less than 100 quanta as the beam scans through the tissue.

Process Time

We used the measured value of the single-shot threshold fluence in a calculation based on a Gaussian beam approximation to estimate the maximum possible ablation rate. For an optimized amplifier that will deliver at

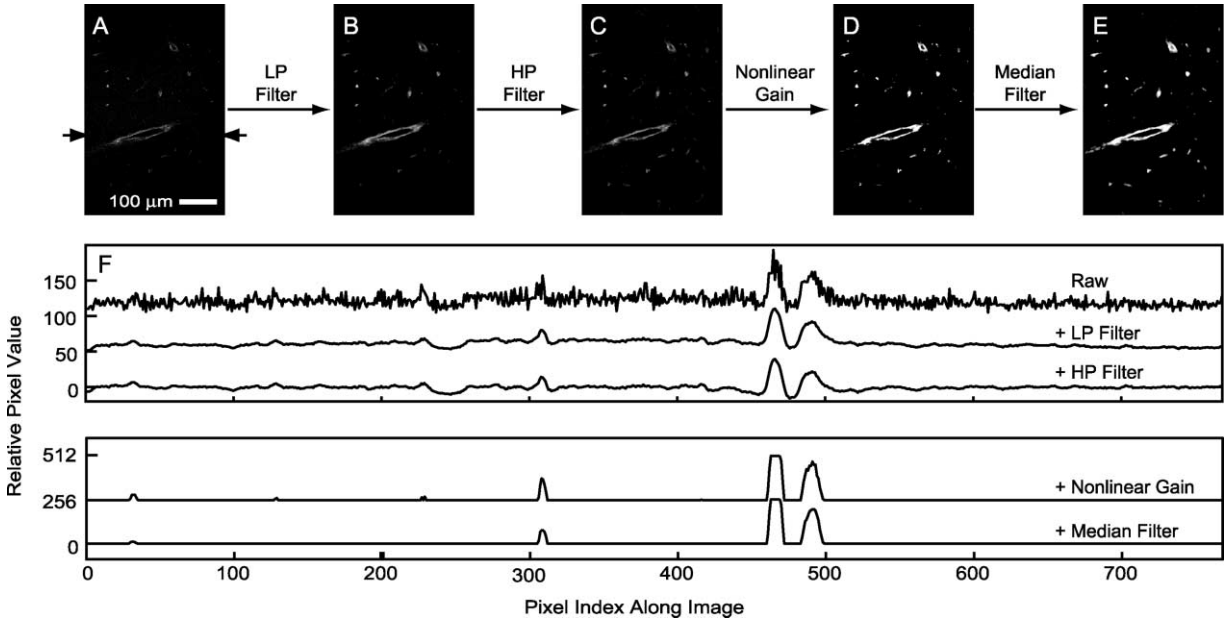

Figure 9. Numerical Processing of Stacks of TPLSM Optical Sections to Form Three-Dimensional Images

(A) A single optical section through the neocortical vasculture of a CFP-labeled transgenic mouse. The lateral resolution is 0.49 μm per pixel.

(B) The same section after low-pass filtering by convolution with a uniform 5 × 5 pixel kernel.

(C) The section after high-pass filtering. An intermediate, low-pass filtered image was constructed by convolving the raw image with a uniform 81 × 81 pixel kernel, and this intermediate image was subtracted from the image in (B).

(D) The section after filtering by a nonlinear gain operation.

(E) The section after two passes of median filtering with a 5 × 5 pixel kernel to remove isolated processed pixels with nonzero values.

(F) Line scans through the level indicated by the arrows in (A). The upper traces in the top box have been offset by 50 pixels while that in the lower box was offset by 256 pixels. Note how the peaks in the signal at the vessel walls are sharpened, and the noise suppressed, between the scans through raw (A) and processed (B–E) sections.

least 10 μJ per pulse of energy at the focus of the objective and which operates at a 20 kHz repetition rate (Backus et al., 2001), the typical volume ablation rate is expected to be 0.02 mm^3/s. This is consistent with and about 50 times faster than the maximum rate in the present work, for which we used amplifiers with 1.0 and 1.2 kHz repetition rates. The image acquisition rate is typically much less than the ablation rate, i.e., one V_{focus} in 0.5 μs, or 0.0005 mm^3/s with the ~1 kHz scanners in the present work. However, with commercially available resonant scanners that operate at 20 kHz, one can achieve one V_{focus} in 0.02 μs, or an imaging rate of 0.01 mm^3/s. The volume of an adult mouse brain is V_{brain} ~400 mm^3 (Franklin and Paxinos, 1997), so that ~18 hr would be required to process an entire mouse brain with an optimized system and fluorophores that are sufficiently bright to achieve a reasonable signal-to-noise ratio in a 0.02 μs pixel dwell time. For completeness, we note that this generates $V_{brain}/V_{focus} \sim 2$ terabytes of uncompressed digital data per marker per mouse brain.

Extensions

We have demonstrated the use of our procedure with image contrast provided by water-soluble stains of nuclear material or the use of intrinsically labeled tissue. An untested extension of the current procedure is the visualization of molecules with bound antibodies to allow high-resolution mapping of protein expression in the brain. One approach could be offline immunostaining of ablated tissue surfaces with directly labeled antibodies and the use of a kinematic mount to reposition tissue between the imaging and ablation steps. An alternative approach involves the in vivo delivery of genetically engineered antibody fragments, such as minibodies and diabodies (Hu et al., 1996; Wu and Yazaki, 2000), as a means to selectively identify specific cell surface receptors. Contrast with these labels depends on the excretion of antibodies fragments that are unbound in addition to the avidity of the fragments. It is tempting to speculate that this technology, currently in use in oncology studies, could provide a means for high-resolution imaging of expression of cell surface molecules throughout the brain.

The ability to localize mRNA or DNA with hybridization probes in the context of our all-optical histology procedure is problematic with current conventional methods of in situ hybridization. However, the burgeoning inventory of transgenic animals that express fluorescently tagged gene products, or coexpress fluorescent proteins with specific gene products, may well justify the utility of the present approach to whole brain histology.

Experimental Procedures

Tissue Preparation

Adult Tissue

Adult animals of both sexes, including Sprague-Dawley rats, NIH Swiss mice, and transgenic mice (see below), were perfused with

phosphate-buffered saline (PBS) for the generation of fresh tissue. The typical perfusion volumes were 0.5 ml per gram animal and flow rates were 20 ml/min. The extracted brain was maintained in an artificial cerebral spinal fluid (Kleinfeld and Delaney, 1996) that was chilled to +7°C and was used immediately for the ablation and imaging procedure. For the case of fixed tissue, the PBS perfusion was immediately followed by a second perfusion with 4% (w/v) paraformaldehyde (PFA) in PBS. The extracted brain was stored in 4% PFA in PBS for postfixation. Blocking of the tissue was done with a mounted razor blade.

Neonatal Tissue

Tissue from day E14 to E15 mouse pups was obtained from pregnant mice that were sacrificed with pentobarbital (50 mg per g mouse). The uteri were removed to an ice-cold solution of PBS and individual mice were dissected, transcardially perfused with PBS followed by 4% PFA in PBS, and stored in fixative prior to photo-ablation.

Transgenic Mice

Neuronal architecture was imaged in mouse strain B6.Cg-TgN(thy1-YFPH)2Jrs (Feng et al., 2000), a transgenic animal with a mosaic expression of YFP in central neurons (No. 003782, The Jackson Laboratory, Bar Harbor, ME). Cortical vasculature was imaged in a novel strain of transgenic mice that expressed the fluorescent chimeric protein, yellow cameleon 3.0 (YC-3.0). Yellow cameleon 3.0 is a tandem fusion of an enchanced cyan-emitting mutant of the green fluorescent protein, a mutant calmodulin, the calmodulin binding peptide M13, and an enhanced yellow-emitting green fluorescent protein (Miyawaki et al., 1997). The mutation of the calmodulin tuned the Ca^{2+} affinity of cameleon to be a sensitive indicator of free Ca^{2+} concentrations in the vicinity of 1 μM. We formed transgenic mice that express YC-3.0 by the introduction of the gene that encodes YC-3.0, along with the β actin and cytomegalovirus promoters. The founders of the line were the hybrid mouse strain C57Bl/6J. We observed mosaic expression of the fluorescent proteins in a manner that was consistent across multiple animals and generations. For the present work, we exploit the preferential labeling of vasculature in the neocortex and Purkinje cells in the cerebellum.

Ablation Techniques

Source

Optimization studies (Figures 3 to 6) were carried out with separate facilities for ablation and imaging. The ablation set-up was based on a Ti:Sapphire regenerative amplifier of local design that produced 100 fs duration, 800 nm wavelength pulses with up to 300 μJ energy at a 1.2 kHz repetition rate (Salin et al., 1991). The pulse energy that was delivered to the sample was controlled with the serial combination of a halfwave plate and polarizing, thin-film beam splitters. A two-lens telescope was used to adjust the diameter of the beam so that it overfilled the back aperture of the objective. Final pulse energies are reported for the focus of the objective.

Tissue reconstruction studies (Figures 7 and 8) were carried out in a composite facility (Figure 2C). A commercially available Ti:Sapphire femtosecond laser oscillator (Mira 900-F pumped by a Verdi V10, Coherent Inc., Santa Clara, CA) that provides the pulses used for two-photon fluorescence imaging is also used to generate seed pulses that are amplified to higher energy for the ablation. A pulse picker, based on a pair of crossed polarizers with a Pockel's cell between them, currently selects one out of every 76,000 pulses for amplification to form a 1 kHz pulse train.

The amplifier is of local design and is based on the chirped-pulse technique (Backus et al., 1998; Strickland and Mourou, 1985). Briefly, seed pulses are first stretched over time using a dispersive delay device based on a grating and telescope. This stretcher is of an all-reflective design and increases the duration of the pulses from 120 fs to approximately 100 ps. These stretched pulses are then directed to a three-mirror ring-shaped Ti:Sapphire multipass amplifier (Backus et al., 1997, 2001). The amplifier crystal is pumped at 1 kHz with 11 mJ, 532 nm pulses from a diode-pumped Nd:YAG laser (Corona, Coherent, Inc.). The seed pulses pass through the pumped region of the crystal eight times and extract energy in each pass. The pulses are then sent through a spatial filter and directed to a dual grating compressor where the dispersion added to the pulse in the stretcher, as well as the dispersion caused by propagation through the optics in the amplifier, is removed. The pulses that emerge from the amplifier are approximately 120 fs in duration with an energy of up to 400 μJ and have a smooth spatial profile.

Polarization optics are used to bring both the amplified, ablation beam and the unamplified, imaging beam into the same microscope. A polarizing beamsplitter cube is inserted between the tube lens and objective in the microscope at an orientation that allows the imaging beam to pass through (Figure 2C). The ablation beam passes through a halfwave plate to make its polarization orthogonal to the imaging beam and is directed off of the polarizer and aligned to be collinear with the imaging beam. The energy of the amplified laser pulses is controlled with neutral density filters. A pair of telescopes located before the microscope controls the size and divergence of both the imaging and ablating beams. Fine adjustment of these telescopes and the alignment allows the focus of the imaging and ablation beams to be made coincident. The ablation beam typically overfills the back aperture of the objective, while the imaging beam just fills the aperture.

Cutting

All tissue ablations, with the exception of the fine channels in cortical tissue shown in Figure 3D, were carried out in an aqueous environment. Fixed tissue ablations were carried out under a 1 to 3 mm layer of PBS that maintained the moisture of the tissue sample and, for the case of water-immersion objectives, formed a continuous layer with the lens. Hydrolysis bubbles, a byproduct of ablation in aqueous media (Noack et al., 1998; Schaffer et al., 2002), were removed by routinely breaking and reforming the aqueous contact with the objective. All cutting was at room temperature. In contrast, for fresh tissue the ablations were carried out in ACSF and maintained between 7°C and 10°C by chilled-water heat-exchange. Lastly, for the single case of nonaqueous ablation (Figure 3D), the tissue was maintained at high humidity by partially enclosing the ablation chamber and purging it with air that was humidified through an aqueous bubbling chamber.

Ablation involved gating the amplified laser pulses onto the sample and translating the sample underneath the objective. Positioning was controlled by an X-Y computer-driven motorized translation stage (no. 1035LT-DC2/E1000AS with Unidex 11 controller, Aerotech, Pittsburgh, PA). In some cases, for increased ablation overlap, ablation channels were laterally interlaced between axial planes. Axial translation of the focus was achieved by moving the micrometer-mounted objective holder along a vertically mounted rail.

Visualization

Staining

Subsequent to ablation, tissues were stained either with the lipid analog 5-hexadecanoylamino-fluorescein (no. 23,547-4, Aldrich) to visualize the cell membranes or with the nucleic acid stain acridine orange (no. H-110, Molecular Probes) to emphasize the somata. The 5-hexadecanoylamino-fluorescein was prepared as a 50 μM solution in 1% (v/v) ethanol in ACSF solution. The stain was bath applied for 3 min followed by 4 to 5 brief washes with PBS. The acridine orange was prepared as a 100 μM solution in 0.1% (v/v) HCl in deionized water. This stain was also bath applied for 3 min followed by 5 brief washes with PBS.

Imaging

Optical sectioning of all samples was performed with an upright two-photon laser scanning microscope of local design (Tsai et al., 2002). We used a 40× magnification, 0.80 NA water immersion objective (Carl Zeiss, Inc., Thornwood, NY) to obtain all data, with the exception of the high-magnification embryonic image (Figure 5F), for which we used a 100× magnification, 1.0 NA water immersion objective (Olympus America, Inc., Melville, NY). Software control of the microscope and data acquisition utilized code that was written in LabView™ (National Instruments, Austin, TX). An ablation apparatus has been incorporated into the microscope, as shown schematically in Figure 2C. This scheme allows for the iterative processing of tissue while maintaining absolute tissue coordinates. For practical reasons, samples used for the optimization studies (Figures 3–6) were placed in a kinematic mount and moved between ablation and imaging set-ups that were separated by 10 m.

Immunostaining

In preparation for immunostaining, photo-ablated tissue was stored in fixative and then cryoprotected with 30% (w/v) sucrose in phos-

phate buffer. The tissue was sectioned on a freezing sliding microtome along a saggital plane that ran perpendicular to the optically cut surface. The sample thickness was 25 μm.

The tissue sections were incubated for 2 days at room temperature in primary antibody directed against tyrosine hydroxylase (1:1000 dilution) (AB151, Chemicon, Temecula, CA) in antibody diluent comprised of 5% (v/v) serum (S1000, Vector Laboratories, Burlingame, CA), 1% (v/v) triton X-100 detergent (T-8787, Sigma), and 0.1% (w/v) sodium azide. After 5 washes in PBS, the sections were transferred to biotinylated peroxidase-conjugated secondary antibody (1:1000 dilution) (BA-1000; Vector Laboratories) in antibody diluent for 2 hr. Sections were again washed and next transferred to an avidin-biotin solution (PK-6100; Vector Laboratories). The bound complex was visualized with diaminobenzodine (SK-4100; Vector Laboratories). The sections were mounted on gelatin-coated slides, dehydrated through graded alcohols into xylenes, and cover-slipped with DPX synthetic resin mounting media (36029F, Gallard-Schlesinger, Garden City Long Island).

Determination of Surface Smoothness

The analysis of surface smoothness (Figures 3E–3G) was carried out on tissue samples that were physically sectioned with either ultrashort laser pulses, a Vibratome™ (System 1000 with no. 121-4 blade, Ted Pella, Inc., Redding, CA), or a cryostat (Jung FrigoCut 2800E, Leica Microsystems Heidelberg, Gemany, with C-profile knife from Microm, Walldorf, Germany). The sectioned surface was then stained by bath application of the lipid analog 5-hexadecanoylamino-fluorescein, as described above, and transected with a mounted razor blade along a plane perpendicular to the sectioned surface. The tissue was then mounted so that TPLSM could be used to acquire optical sections that included successive scans through the razor cut surface. We typically acquired scans in 0.5 μm axial intervals throughout a depth 50 μm into the tissue.

We focused on square regions, typically 200 × 200 pixels in size, that were centered on the laser-cut surface. The data were processed to extract a cross-section of the physical cut, from which we estimated the root-mean-square (RMS) variation in the height of the cut. Our processing involved three steps: First, the data were low-pass filtered by convolution with a 3 × 3 pixel kernel. Second, we fit step functions to each of 200 lines of pixels that passed through the cut. The high and low values of the step were defined as the median values of the tissue fluorescence versus unlabeled void, respectively. The position of the steps defined the height variations of the physical step along a 200 pixel line. Finally, the standard deviation was calculated from these variations, and the results for all sections were compiled together to generate a single standard deviation value, denoted δz_{RMS}.

Volume Reconstruction

Individual optical sections (Figure 9A) were filtered to suppress noise and enhance contrast. The intensities of the separate sections were then normalized to permit volumetric operations. Our filtration involved four steps. First, the background noise, which was approximately white and Gaussian, was effectively suppressed by low-pass filtering. We chose a 5 × 5 pixel (0.49 μm/pixel) square averaging kernel that was convolved with the data in each section, and we used reflecting boundaries to minimize edge effects (Figures 9B and 9F). Second, the nonuniformity within each section was corrected by high-pass filtering (Figures 9C and 9F). This operation involved subtraction of a heavily low-pass filtered version of the section, i.e., 81 × 81 pixel averaging kernel with reflecting boundaries, from the unfiltered data. Third, normalization of the data, along with suppression of the noise, was accomplished by a nonlinear mapping of the form

$$x \leftarrow \begin{cases} 0 & \text{if} \quad x \le \theta \\ G\dfrac{(x-\theta)}{max(x)} & \text{if} \quad \theta \le x < \theta + G^{-1}\,max(x), \\ 1 & \text{if} \quad x > G + \theta \end{cases}$$

where x is the value of the pixel, θ is the noise level (θ = 5 for our 8-bit data), and G is a gain factor (G = 4.0 for the present data sets) (Figures 9D and 9F). The resulting images have a large portion of pixels set to zero. The fourth and final step was to apply a double median filter, using a 5 × 5 square kernel of pixels, as a means to smooth edges, fill small voids, i.e., areas of low pixel value surrounded by larger areas of high pixel value, and remove isolated bright spots, i.e., small areas of nonzero values (Figures 9E and 9F). For volumetric realization, the processed image stack was rendered with the use of a ray-casting algorithm (XVOLUME, Interactive Display Language, Research Systems Inc., CO).

The volume fraction associated with the reconstructed vasculature (Figure 8E) was estimated from the processed stack of sections with the assumption that bright voxels are associated with blood vessel walls. We applied a threshold to each voxel to create a binary image that indicated the likely locations of the vessel walls. We then filled all voids, i.e., areas that are completely surrounded by vessel walls. The resulting processed image indicates both vessel walls and interior, from which we compute the fraction of voxels that are associated with blood vessels and blood.

Appendix

We can estimate the volume of the ablated material in terms of the energy of the incident pulses and a phenomenological value for the threshold fluence of ablation (Figures 3A and 3B). Noting from standard texts (Yariv, 1985) that the intensity for a Gaussian beam that propagates along the *z* axis, I(r, z, t), can be written in the form

$$I(r,z,t) = 2\left(\frac{P(t)}{\pi w^2(z)}\right)e^{-2r^2/w^2(z)},$$

where P(t) is the power, w(z) is the radius of the beam, and the energy per pulse is

$$E = \int_{-\infty}^{\infty} dt \int_{0}^{\infty} r\,dr \int_{-\pi}^{\pi} d\theta\, I(r,0,t).$$

The relevant parameterization for cutting is the fluence,

$$F(r,z) = \int_{-\infty}^{\infty} dt\, I(r,z,t) = 2\left[\frac{E}{\pi w^2(z)}\right]e^{-2r^2/w^2(z)}.$$

The dependence of the fluence on the axial distance *z* is simplified for the paraxial approximation, valid for NA << n where n is the index of refraction (n = 1.3 for saline), i.e.,

$$w(z) = w_0\sqrt{1 + \left(\frac{NA}{n}\frac{z}{w_0}\right)^2},$$

for which $w_0 = \lambda/(\pi NA)$ is the radius of a diffraction limited spot at the focus. We denote the threshold value of the fluence at the focus as F_T. The extent of the ablated region along the *z* axis, denoted z_T, is found from $F_T = 2[E/[\pi w^2(z_T)]]$, for which

$$z_T = w_0\left(\frac{n}{NA}\right)\sqrt{\epsilon - 1},$$

where $\epsilon = (2E)/(\pi w_0^2 F_T)$ is the normalized energy per pulse and ablation requires $\epsilon > 1$. The ablation volume with the focal plane at the surface of the tissue is given by

$$V = \int_{-z_T}^{0} dz\, \pi r^2(z)$$

$$= \frac{\pi}{2}\left(\frac{n}{NA}\right)w_0^3\int_{0}^{x_T} dx\,(1 + x^2)\,ln\left(\frac{1 + x_T^2}{1 + x^2}\right),$$

where r(z) is the radius for which the fluence of the beam equals F_T, and we inverted the expression for F(r,z) and normalized the integration variable, with $X_T = \sqrt{\epsilon - 1}$. Although the integral can be done exactly, extrapolation beyond the threshold fluence is appropriate only for small values of x_T or, equivalently, for ε close to 1. We find

$$V \xrightarrow[\epsilon \approx 1]{} \left(\frac{\pi}{9}\right)\left(\frac{n}{NA}\right)w_0^3(\epsilon - 1)^{3/2},$$

which corresponds to an ellipsoidal crater of height z_T and radius

$$r_T = w_0\sqrt{(\epsilon - 1)/6}, \text{ with } z_T/r_T = \sqrt{6}\left(\frac{n}{NA}\right) \approx 6 \text{ to } 16$$

for the objectives used in our study. At high energies, i.e., $\epsilon >> 1$, or for focal planes deep to the surface of the tissue, one needs to take into account the decrement in energy as the pulse propagates into the sample and creates a plasma.

Acknowledgments

We dedicate this paper to the memory of our colleague, Kent Wilson, who sparked this collaborative effort. We thank Jerold Chun for the use of his cryostat, Earl Dolnick and Allen White for assistance with instrumentation, Shannon Hefler for assistance with tissue preparation, and Harvey Karten for expert instruction on photomicroscopy. We further thank Coherent, Inc. and Olympus America, Inc., for the loan of equipment. This work was supported by awards from the Burroughs Wellcome Fund (La Jolla Interfaces in Science training award to C.B.S.), the David and Lucille Packard Foundation (D.K.), the Howard Hughes Medical Institute (R.Y.T.), the National Institutes of Health (training grant PHS/33201A/T32MH20002 for P.S.T. and research grants NS/041096 to D.K. and NS/27177 to R.Y.T.), and the National Science Foundation (POWRE grant 0074776 to B.F. and research grant DBI/9987257 to J.A.S.).

Received: January 17, 2003
Revised: May 16, 2003
Accepted: June 6, 2003
Published: July 2, 2003

References

Ashcom, J.B., Schaffer, C.B., and Mazur, E. (2002). Numerical aperture dependence of damage and white light generation from femtosecond laser pulses in bulk fused silica. In Commercial and Biomedical Applications of Ultrafast and Free-Electron Lasers (San Jose, CA: International Society for Optical Engineering), pp. 107–111.

Backus, S., Durfee, C.G., III, Mourou, G., Kapteyn, H.C., and Murnane, M.M. (1997). 0.2-TW laser system at 1 kHz. Opt. Lett. *22*, 1256–1258.

Backus, S., Durfee, C.G., III, Murnane, M.M., and Kapteyn, H.C. (1998). High power ultrafast lasers. Rev. Sci. Instrum. *69*, 1207–1223.

Backus, S., Bartels, R., Thompson, S., Dollinger, R., Kapteyn, H.C., and Murnane, M.M. (2001). High-efficiency, single-stage 7-kHz high-average-power ultrafast laser system. Opt. Lett. *26*, 465–467.

Bestvater, F., Spiess, E., Stobrawa, G., Hacker, M., Feurer, T., Porwol, T., Berchner-Pfannschmidt, U., Wotzzlaw, C., and Acker, H. (2002). Two-photon fluorescence absorption and emission spectra of dyes relevant for cell imaging. J. Micros. *208*, 108–115.

Cooper, J.R., Bloom, F.E., and Roth, R.H. (1996). The Biochemical Basis of Neuropharmacology (New York: Oxford University Press).

Denk, W., and Svoboda, K. (1997). Photon upmanship: why multiphoton imaging is more than a gimmick. Neuron *18*, 351–357.

Denk, W., Strickler, J.H., and Webb, W.W. (1990). Two-photon laser scanning fluorescence microscopy. Science *248*, 73–76.

Du, D., Liu, G., Korn, G., Squier, J., and Mourou, G. (1994). Laser-induced breakdown by impact ioization in SiO_2 with pulse widths from 7 ns to 150 fs. Appl. Phys. Lett. *64*, 3071–3073.

Eltoum, I.A., Siegal, G.P., and Frost, A.R. (2002). Microdissection of histological sections: past, present, and future. Adv. Anat. Pathol. *9*, 316–322.

Feng, G., Mellor, R.H., Bernstein, M., Keller-Peck, C., Nguyen, Q.T., Wallace, M., Nerbonne, J.M., Lichtman, J.W., and Sanes, J.R. (2000). Imaging neuronal subsets in transgenic mice expressing multiple spectral variants of GFP. Neuron *28*, 41–51.

Franklin, K.B.J., and Paxinos, G. (1997). The Mouse Brain in Stereotaxic Coordinates (San Diego, CA: Academic Press).

Frederickson, K.S., White, W.E., Wheeland, R.G., and Slaughter, D.R. (1993). Precise ablation of skin with reduced collateral damage using the femtosecond-pulsed, terawatt titanium-sapphire laser. Arch. Dermatol. *129*, 989–993.

Goetz, M.H., Fischer, S.K., Velten, A., Bille, J.F., and Strum, V. (1999). Computer-guided laser probe for ablation of brain tumours with intrashort laser pulses. Phys. Med. Biol. *44*, N119–N127.

Grutzendler, J., Kasthuri, N., and Gan, W.B. (2002). Long-term dendritic spine stability in the adult cortex. Nature *420*, 812–816.

Harrison, R.V., Harel, N., Panesar, J., and Mount, R.J. (2002). Blood capillary distribution correlates with hemodynamic-based functional imaging in cerebral cortex. Cereb. Cortex *12*, 225–233.

Hu, S., Shively, L., Raubitschek, A., Sherman, M., Williams, L.E., Wong, J.Y., Shively, J.E., and Wu, A.M. (1996). Minibody: a novel engineered anti-carcinoembryonic antigen antibody fragment (single-chain Fv-CH3) which exhibits rapid, high-level targeting of xenografts. Cancer Res. *56*, 3055–3061.

Juhasz, T., Loesel, H.L., Kurtz, R.M., Horvath, C., Bille, J.F., and Mourou, G. (1999). Corneal refractive surgery with femtosecond lasers. IEEE J. Select. Top. Quant. Elect. *5*, 902–910.

Kleinfeld, D., and Delaney, K.R. (1996). Distributed representation of vibrissa movement in the upper layers of somatosensory cortex revealed with voltage sensitive dyes. J. Comp. Neurol. *375*, 89–108; erratum (1997). *378*, 594.

Kleinfeld, D., Mitra, P.P., Helmchen, F., and Denk, W. (1998). Fluctuations and stimulus-induced changes in blood flow observed in individual capillaries in layers 2 through 4 of rat neocortex. Proc. Natl. Acad. Sci. USA *95*, 15741–15746; erratum (1999). *96*, 8307c.

Lendvai, B., Stern, E.A., Chen, B., and Svoboda, K. (2000). Experience-dependent plasticity of dendritic spines in the developing rat barrel cortex in vivo. Nature *404*, 876–881.

Lenzner, M., Kruger, J., Sartania, S., Cheng, Z., Spielmann, C., Mourou, G., Kautek, W., and Krausz, F. (1998). Femtosecond optical breakdown in dielectrics. Phys. Rev. Lett. *80*, 4076–4079.

Levitt, P., Cooper, M.L., and Rakic, P. (1981). Coexistence of neuronal and glial precursor cells in the cerebral ventricular zone of the fetal monkey: an ultrastructural immunoperoxidase analysis. J. Neurosci. *1*, 27–39.

Loesel, F.H., Niemez, M.H., Bille, J.F., and Juhasz, T. (1996). Laser-induced optical breakdown on hard and soft tissues and its dependence on the pulse duration: experiment and model. IEEE J. Quant. Elect. *32*, 1717–1722.

Loesel, F.H., Fischer, J.P., Gotz, M.H., Horvath, C., Juhasz, T., Noack, F., Suhm, N., and Bille, J.F. (1998). Non-thermal ablation of neural tissue with femtosecond laser pulses. Appl. Phys. B *66*, 121–128.

Lubatschowski, H., Maatz, G., Heisterkamp, A., Hetzel, U., Drommer, W., Welling, H., and Ertmer, W. (2000). Application of ultrashort laser pulses for intrastromal refractive surgery. Graefes Arch. Clin. Exp. Opthalmol. *238*, 33–39.

Maatz, G., Heisterkamp, A., Lubatschowski, H., Barcikowski, S., Fallnich, C., Welling, H., and Ertmer, W. (2000). Chemical and physical side effects at application of ultrashort laser pulses for intrastromal refractive surgery. J. Opt. Soc. Am. A *2*, 59–64.

Miyawaki, A., Llopis, J., Heim, R., McCaffery, J.M., Adams, J.A., Ikura, M., and Tsien, R.Y. (1997). Fluorescent indicators for Ca2+ based on green fluorescent proteins and calmodulin. Nature *388*, 882–885.

Momma, C., Chichkov, B.N., Nolte, S., von Alvensleben, F., Tunnermann, A., Welling, H., and Wellegehausen, B. (1996). Short-pulse laser ablation of solid targets. Opt. Commun. *129*, 134–142.

Motti, E.D., Imhof, H.-G., and Yasargil, M.G. (1986). The terminal vasculature bed in the superficial cortex of the rat: an SEM study of corrosion casts. J. Neurosurg. *65*, 834–846.

Neev, J., Da Silva, L.B., Feit, M.D., Perry, M.D., Rubenchik, A.M., and Stuart, B.C. (1996). Ultrashort pulse lasers for hard tissue ablation. IEEE J. Select. Top. Quant. Elect. *2*, 790–800.

Noack, J., Hammer, D.X., Noojin, G.D., Rockwell, B.A., and Vogel, A. (1998). Influence of pulse duration on mechanical effects after laser-induced breakdown in water. J. Appl. Phys. *83*, 7488–7495.

Oheim, M., Beaurepaire, E., Chaigneau, E., Mertz, J., and Charpak, S. (2001). Two-photon microscopy in brain tissue: parameters influencing the imaging depth. J. Neurosci. Meth. *111*, 29–37. Erratum J. Neurosci. Meth. (2001). *112*, 205.

Oraevsky, A., Da Silva, L., Rubenchik, A., Feit, M., Glinsky, M., Perry, M., Mammini, B., Small, W., and Stuart, B. (1996). Plasma mediated ablation of biological tissues with nanosecond-to-femtosecond laser pulses: Relative role of linear and nonlinear absorption. IEEE J. Select. Top. Quant. Elect. *2*, 801–809.

Rakic, P. (1972). Mode of cell migration to the superficial layers of fetal monkey neocortex. J. Comp. Neurol. *145*, 2013–2083.

Rauschning, W. (1986). Surface cryoplaning: a technique for clinical anatomical correlations. Ups. J. Med. Sci. *91*, 251–255.

Salin, F., Squier, J., Mourou, G., and Vaillancourt, G. (1991). Multi-kHz Ti:Sapphire amplifier for high power femtosecond pulses. Opt. Lett. *16*, 1964–1967.

Schaffer, C.B., Nishimura, N., Glezer, E.N., Kim, A.M.-T., and Mazur, E. (2002). Dynamics of femtosecond laser-induced breakdown in water from femtoseconds to microseconds. Opt. Express *10*, 196–203.

Shirk, M.D., and Molian, P.A. (1998). A review of ultrashort pulsed laser ablation of materials. J. Laser Appl. *10*, 19–28.

Strickland, D., and Mourou, G. (1985). Compression of amplified chirped optical pulses. Opt. Commun. *55*, 447–449.

Stuart, B.C., Feit, M.D., Rubenchik, A.M., Shore, B.W., and Perry, M.D. (1995). Laser-induced damage in dielectrics with nanosecond to subpicosecond pulses. Phys. Rev. Lett. *74*, 2248–2251.

Stuart, B.C., Feit, M.D., Herman, S., Rubenchik, A.M., Shore, B.W., and Perry, M.D. (1996). Nanosecond-to-subpicosecond laser-induced breakdown in dielectrics. Phys. Rev. B Condens. Matter *53*, 1749–1761.

Suhm, N., Gotz, M.H., Fischer, J.P., Loesel, F., Schlegel, W., Sturm, V., Bille, J.F., and Schroder, R. (1996). Ablation of neural tissue by short-pulsed lasers—a technical report. Acta Neurochir. *138*, 346–349.

Svoboda, K., Denk, W., Kleinfeld, D., and Tank, D.W. (1997). In vivo dendritic calcium dynamics in neocortical pyramidal neurons. Nature *385*, 161–165.

Takahashi, T., Nowakowski, R.S., and Caviness, V.S.J. (1995). Mode of cell proliferation in the developing mouse neocortex. Proc. Natl. Acad. Sci. USA *91*, 375–379.

Tirlapur, U.K., and Konig, K. (2002). Targeted transfection by femtosecond laser light. Nature *418*, 290–291.

Toga, A.W., Ambach, K., Quinn, B., Hutchin, M., and Burton, J.S. (1994). Postmortem anatomy from cryosectioned whole human brain. J. Neurosci. Methods *54*, 239–252.

Toga, A.W., Goldkorn, A., Ambach, K., Chao, K., Quinn, B.C., and Yau, P. (1997). Postmortem cryosectioning as an anatomic reference for human brain mapping. Comput. Med. Imaging Graph. *21*, 131–141.

Tsai, P.S., Nishimura, N., Yoder, E.J., Dolnick, E.M., White, G.A., and Kleinfeld, D. (2002). Principles, design, and construction of a two photon laser scanning microscope for in vitro and in vivo brain imaging. In In Vivo Optical Imaging of Brain Function, R.D. Frostig, ed. (Boca Raton, FL: CRC Press), pp. 113–171.

Wu, A.M., and Yazaki, P.J. (2000). Designer genes: recombinant antibody fragments for biological imaging. Q. J. Nucl. Med. *44*, 268–283.

Xu, C., and Webb, W.W. (1996). Measurement of two-photon excitation cross sections of molecular fluorophores with data from 690 to 1050 nm. J. Opt. Soc. Am. B *13*, 481–491.

Xu, C., Zipfel, W., Shear, J.B., Williams, R.M., and Webb, W.W. (1996). Multiphoton fluorescence excitation: new spectral windows for biological nonlinear microscopy. Proc. Natl. Acad. Sci. USA *93*, 10763–10768.

Yariv, A. (1985). Optical Electonics, Third Edition (New York: Holt, Rinehart and Wilson).

Yuste, R., and Denk, W. (1995). Dendritic spines as basic functional units of neuronal integration. Nature *375*, 682–684.